Journal of Power Sources 196 (2011) 7797–7805

Contents lists available at ScienceDirect

Journal of Power Sources

journal homepage: www.elsevier.com/locate/jpowsour

Comparative structural and electrochemical study of high density spherical and non-spherical $Ni(OH)_2$ as cathode materials for Ni–metal hydride batteries

Enbo Shangguan[a], Zhaorong Chang[a,b,*], Hongwei Tang[a], Xiao-Zi Yuan[b], Haijiang Wang[b]

[a] College of Chemistry and Environmental Science, Henan Normal University, Xinxiang 453007, PR China
[b] Institute for Fuel Cell Innovation, National Research Council of Canada, Vancouver, BC, Canada V6T 1W5

ARTICLE INFO

Article history:
Received 13 January 2011
Received in revised form 9 April 2011
Accepted 10 May 2011
Available online 18 May 2011

Keywords:
Nickel hydroxide
High-density
Nickel–metal hydride batteries
High-rate discharge
Cathode materials

ABSTRACT

In this paper we compare the behavior of non-spherical and spherical β-$Ni(OH)_2$ as cathode materials for Ni–MH batteries in an attempt to explore the effect of microstructure and surface properties of β-$Ni(OH)_2$ on their electrochemical performances. Non-spherical β-$Ni(OH)_2$ powders with a high-density are synthesized using a simple polyacrylamide (PAM) assisted two-step drying method. X-ray diffraction (XRD), infrared spectroscopy (IR), scanning electron microscopy (SEM), thermogravimetric/differential thermal analysis (TG–DTA), Brunauer–Emmett–Teller (BET) testing, laser particle size analysis, and tap-density testing are used to characterize the physical properties of the synthesized products. Electrochemical characterization, including cyclic voltammetry (CV), electrochemical impedance spectroscopy (EIS), and a charge/discharge test, is also performed. The results show that the non-spherical β-$Ni(OH)_2$ materials exhibit an irregular tabular shape and a dense solid structure, which contains many overlapped sheet nano crystalline grains, and have a high density of structural disorder and a large specific surface area. Compared with the spherical β-$Ni(OH)_2$, the non-spherical β-$Ni(OH)_2$ materials have an enhanced discharge capacity, higher discharge potential plateau and superior cycle stability. This performance improvement can be attributable to a higher proton diffusion coefficient (4.26×10^{-9} cm^2 s^{-1}), better reaction reversibility, and lower electrochemical impedance of the synthesized material.

1. Introduction

As a result of excellent electrochemical properties, nickel hydroxide ($Ni(OH)_2$) has been intensively studied and widely used as a cathode material in all nickel-based alkaline secondary cells [1–5]. Generally, there exist two nickel hydroxide polymorphs: α-phase $Ni(OH)_2$ and β-phase $Ni(OH)_2$, which can be transformed into γ-phase NiOOH and β-phase NiOOH, respectively, after a full charging [5]. Although α-$Ni(OH)_2$ has a higher theoretical electrochemical capacity, it is very unstable in a strong alkaline medium and easily transforms to β-phase after a few cycles. Moreover, α-$Ni(OH)_2$ exhibits a lower tap density (<1.7 g cm^{-3}), which greatly limits its practical use. The higher tap density can enhance the addition amount of positive material and promote the specific energy density of Ni–MH batteries further. Owing to its high tap density (2.1–2.2 g cm^{-3}) and excellent electrochemical performance, spherical β-$Ni(OH)_2$ has been widely used as a cathode material in commercial Ni–MH batteries [6,7]. However, the preparation procedures for spherical particles are rather complex and the precipitated nickel hydroxide requires aging for a long time to obtain the desired product, which result in the high production cost. Besides, the effective electrode capacity of the spherical β-$Ni(OH)_2$ sample still has room to improve as compared with the theoretical value (289 mAh g^{-1}).

It is well established that the physical properties of nickel hydroxide, such as its morphology, particle-size distribution, tap-density, and specific surface area, chemical composition, are strongly related to performance of the positive electrodes for its practical application in Ni–MH batteries [8–10]. Given the importance of nickel hydroxide to the battery industry, considerable effort has been devoted to improving the performance of the positive electrodes, including: enhancing the stability of the α-phase [11], cationic substitution [7], additives [12], surface modification [2,13] and nanosized materials [5,14–16]. It is noticed that extensive researches are conducted on the preparation and electrochemical performance of nano-$Ni(OH)_2$ in certain applications [14–20]. The discharge capacity of nano-$Ni(OH)_2$ electrodes prepared by ultrasonic chemistry, hard template method and other common methods can reach as high as 250–270 mAh g^{-1}. However, nano-$Ni(OH)_2$ can hardly meet the requirements of industrial mass production [21]. Especially, the nano-particles always exhibit a lower tap density (<1.0 g cm^{-3}) [14], which will result in a low

* Corresponding author at: College of Chemistry and Environmental Science, Henan Normal University, Xinxiang 453007, PR China. Tel.: +86 37333263 35; fax: +86 373 332 6336.
E-mail address: czr_56@163.com (Z. Chang).

0378-7753/$ – see front matter © 2011 Elsevier B.V. All rights reserved.
doi:10.1016/j.jpowsour.2011.05.013

Table 1
The chemical compositions and physical properties of $Ni(OH)_2$ samples A (non-spherical) and B (spherical).

Sample	Chemical composition (wt.%)			BET surface area ($m^2\ g^{-1}$)	Mean diameter (μm)	Tap-density ($g\ cm^{-3}$)
	Ni	Co	Zn			
A (non-spherical)	57.68	1.54	3.13	75.62	27.20	2.22
B (spherical)	57.95	1.51	3.09	10.15	9.34	2.20

volumetric specific capacity, thus seriously limiting the energy density of Ni–MH batteries.

Recently, a polyacrylamide (PAM) assisted two-step drying method has been reported as a simpler method to synthesize high density non-spherical $Ni(OH)_2$ powders [22]. The procedures for non-spherical powders are much simpler than those for spherical powders, more economical with no hydroxide-forming step, and more environmentally friendly with no ammonium involved. The $Ni(OH)_2$ powders prepared by the new method has demonstrated not only a high tap density, but also excellent electrochemical performance. But till now, non-spherical $Ni(OH)_2$ has attracted little attention as raw material for the positive electrode in commercial batteries because non-spherical powders always show a lower tap-density (1.5–1.8 $g\ cm^{-3}$) [8,23]. Most studies about non-spherical $Ni(OH)_2$ in the literature mainly focused on either the properties of $Ni(OH)_2$ electrodes for rechargeable Cd–Ni and Ni–MH batteries or the crystal chemistry of $Ni(OH)_2$ [24–27]. In the previous work [22], we have studied the effect of tap-density on the electrochemical performance of non-spherical $Ni(OH)_2$ electrodes. Nevertheless, it is necessary to compare non-spherical $Ni(OH)_2$ with commercial spherical $Ni(OH)_2$ product and improve the performance of non-spherical $Ni(OH)_2$ before the material can be used in commercial cells. Hence, the goal of this work is to further investigate the structural and electrochemical performance of non-spherical, Co and Zn doped $Ni(OH)_2$ prepared by the polyacrylamide (PAM) assisted two-step drying method in comparison with spherical commercial $Ni(OH)_2$ product with a focus on exploring the effect of microstructure and surface properties of β-$Ni(OH)_2$ with a high tap density on their electrochemical performances.

On the basis of our previous work [22], high density, non-spherical, Co and Zn doped β-$Ni(OH)_2$ was prepared by the polyacrylamide (PAM) assisted two-step drying method. This study focuses on the comparison of structural and electrochemical performance between as-prepared non-spherical β-$Ni(OH)_2$ and commercial spherical β-$Ni(OH)_2$ as cathode materials for Ni–MH batteries. Effects of the microstructure and surface properties of the prepared β-$Ni(OH)_2$ on its electrochemical performance are discussed in detail.

2. Experimental

2.1. Synthesis of $Ni(OH)_2$ powders

Synthesis of non-spherical $Ni(OH)_2$ powders was carried out by the polyacrylamide (PAM) assisted two-step drying method as described previously [22]. Stoichiometric amounts of $NiSO_4{\cdot}6H_2O$, $CoSO_4{\cdot}7H_2O$, $ZnSO_4{\cdot}7H_2O$ (molar ratio of Ni:Co:Zn is 100:2.5:5) were dissolved in distilled water to create a concentration of 1.7 mol L^{-1}. The aqueous solution was precipitated by adding a NaOH solution of 4 mol L^{-1} with continuous stirring at 50 °C. The co-precipitation mixtures were stirred continuously after the reaction ceased, and then coagulated by adding PAM (10 ml PAM (0.6%) per 200 ml solution), filtrated (under a pressure of 20 MPa), dried (at 120 °C for 2 h), ground, washed, and dried (at 120 °C for 2 h) to obtain the final product.

The spherical β-$Ni(OH)_2$ used in this work is a commercial product (Henan Kelong Co., Ltd., China) co-precipitated with 1.5 wt.% Co and 3 wt.% Zn.

2.2. Characterization of $Ni(OH)_2$

The crystalline structure characterization of $Ni(OH)_2$ powders was performed on the X-ray Diffractometer (D8 X) with Cu Kα as irradiation, utilizing a work voltage of 40 kV, a work current of 40 mA, a scanning speed of 0.026° s^{-1} and a step time of 3 s. The scanning range was between 15° and 70°. The sample morphologies were observed using an SEM (SEM-6701F, JEOL, Japan) with a work voltage of 15.00 kV, and the Fourier transform infrared (FTIR) spectra of prepared samples was recorded by a Fourier infrared spectrometer (FIRS; Bio-Rad FTS-40, US) using the KBr pellet method. Thermogravimetric/differential thermal analysis (TG/DTA) was carried out using a Shimadzu DT-40 thermal analyzer (Japan). The measurement was performed in an air flow using α-Al_2O_3 as the reference material. To determine the tap density of the sample, a JZ-1 tap-density tester (Chendu Powder Test Equipment Co., Ltd., China) was used. The measurement error was less than 1%. The specific surface area was evaluated by the BET nitrogen adsorption method using a 3H-2000 surface area analyzer (China). The particle size distribution of the powder samples was obtained using an OMEC LS-POP(III) particle size analyzer (China).

2.3. Preparation of nickel electrodes and electrochemical measurements

Porous foamed nickel was cut into 2 cm × 2 cm to use as substrate material. The pasted nickel electrodes were prepared as follows: 80 wt.% nickel hydroxide, 5 wt.% CoO, 10 wt.% Ni powder were mixed thoroughly with a certain amount of 5 wt.% PTFE solution to obtain a homogeneous slurry possessing adequate rheological properties. The slurry was poured into a foam nickel sheet and dried at 80 °C for 5 h. Subsequently, the pasted electrodes were pressed at 20 MPa for 3 min to assure good electrical contact between the foam nickel and the active material.

Electrochemical tests were performed in a three-compartment electrolysis cell at ambient temperature. Two nickel ribbon counter electrodes were placed in the side chambers and the working electrode was positioned in the center. The geometrical surface area of the nickel electrode was 0.25 cm^2. The electrolyte was a solution of 6 M KOH + 15 g L^{-1} LiOH. A Hg/HgO reference electrode was used via a luggin capillary with the same alkaline solution used in the working cell. CV and EIS were conducted on a Solartron SI 1260 impedance analyzer with a 1287 potentiostat interface. The CV test scan rate was between 1 mV s^{-1} and 8 mV s^{-1} and the cell potential ranged from 0.0 V to 0.8 V. For EIS, the impedance spectra were recorded at a 5 mV perturbation amplitude with a sweep frequency range of 10 kHz–1 mHz.

Test cells were assembled using the prepared nickel hydroxide electrode as the cathode, a hydrogen storage alloy electrode as the anode, and polypropylene to separate the cathode and anode. The electrolyte was a solution of 6 M KOH + 15 g L^{-1} LiOH.

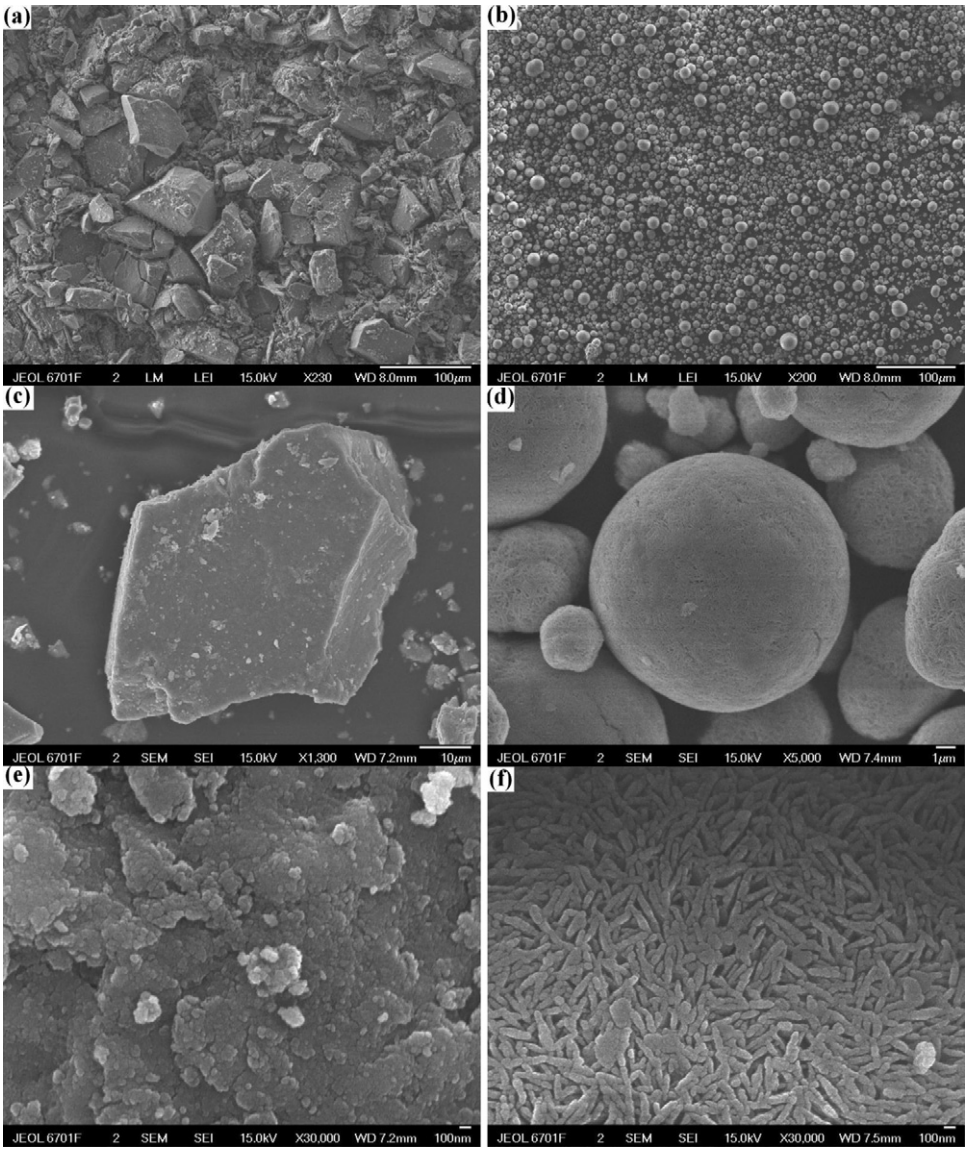

Fig. 1. SEM images of non-spherical $Ni(OH)_2$ (a, c, e) and spherical $Ni(OH)_2$ (b, d, f) at different magnifications.

Charge/discharge measurements were conducted using a Land CT2001A battery performance testing instrument (Wuhan Jinnuo Electronics Co., Ltd., China). For activation, five charge discharge cycles at 0.1 C were performed, and the batteries were discharged to 1.0 V. The batteries were then charged at a 0.2 C rate for 6 h and separately discharged at respective 0.2, 1, 2, and 5 C discharge current rates. The cut-off voltages were set as 0.9 V. In the subsequent charge/discharge cycling tests, the batteries were charged at a 1 C rate for 1.2 h, rested for 10 min, and then discharged at 1 C rate to a limited voltage of 1.0 V. The discharge capacity of the nickel hydroxide in the positive electrode was based on the amount of active material ($Ni(OH)_2$) without taking into account the additives in the electrode.

3. Results and discussion

3.1. Characterization of $Ni(OH)_2$

3.1.1. Physical properties

Critical physical properties of nickel hydroxide powder, including tap density, particle shape, particle size, chemical composition, strongly affect the performance of the positive electrodes. The chemical compositions and physical properties of $Ni(OH)_2$ samples A (non-spherical) and B (spherical) are presented in Table 1.

The cobalt and the zinc contents are almost the same in both samples. The tap-densities of samples A and B are as high as 2.22 and 2.20 g cm^{-3}, respectively. It is worth noting that in order to

Table 2
FWHM, *d*-values in (0 0 1), (1 0 0), (1 0 1) diffraction lines of $Ni(OH)_2$ samples A (non-spherical) and B (spherical).

Sample	(0 0 1)		(1 0 0)		(1 0 1)	
	$FWHM_{001}$ (°)	d_{001} (nm)	$FWHM_{100}$ (°)	d_{100} (nm)	$FWHM_{101}$ (°)	d_{101} (nm)
A (non-spherical)	0.970	0.46866	0.638	0.27059	1.057	0.23411
B (spherical)	0.594	0.46548	0.379	0.27045	0.782	0.23336

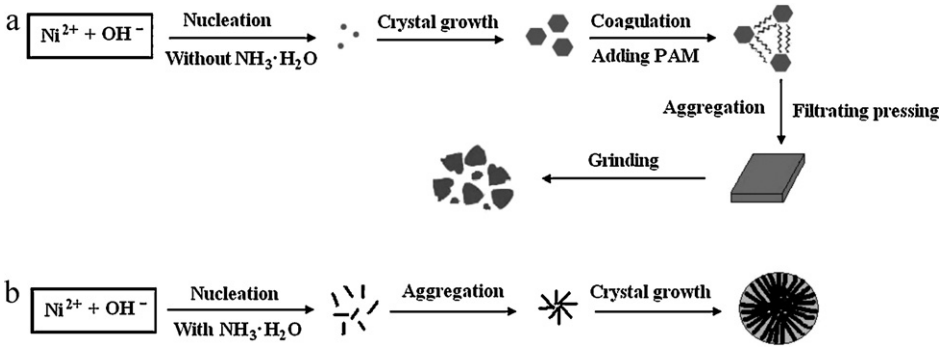

Fig. 2. Schematic illustration of the synthesis process of (a) non-spherical $Ni(OH)_2$ and (b) spherical $Ni(OH)_2$.

explore the effects of microstructure and surface properties of β-$Ni(OH)_2$ on its electrochemical performances, we choose the non-spherical sample with a tap density as high as the spherical one to avoid the effect of tap density, which is not just a particular case. The mean diameters of samples A and B are 27.20 and 9.34 μm, and BET surface areas are 75.62 and 10.15 $m^2 g^{-1}$, respectively. It is noticed that although both samples have almost the same high density, the specific surface area of non-spherical powders is seven times larger than that of the spherical samples, which should be attributed to the irregular particle shape [8]. The higher specific surface area can provide a high density of active sites and thereby promotes intimate interaction between the active material and the surrounding electrolyte.

3.1.2. SEM

Fig. 1(a–f) displays SEM photographs of spherical and non-spherical $Ni(OH)_2$ materials at different magnifications. The powders in Fig. 1a, c and e are sample A (non-spherical $Ni(OH)_2$), and the powders in Fig. 1b, d and f are sample B (spherical $Ni(OH)_2$). From Fig. 1a and c, it is observed that sample A appears to be aggregates of irregular tabular shapes, similar to the ball milled powders. The irregular shapes may result from grinding, which leads to a higher specific surface area and more structural disorder, as shown in Tables 1 and 2. The higher magnification (30,000×) presented in Fig. 1e, shows that each non-spherical particle contains many overlapped sheet nano crystalline grains, which result in a dense solid structure. So, It is believed that the high tap-density of non-spherical $Ni(OH)_2$ is attributable to the dense solid structure.

As can be seen in Fig. 1b and d, sample B is composed of well-dispersed homogeneous spherical particles. Each spherical particle contains a large amount of cuneiform or claviform nano particles of 50–100 nm in width and 100–500 nm in length. As shown in Fig. 1f, these nano crystallites are intercrossed and overlapped, resulting in a radial network microstructure with a large number of pores [28]. When the powders are mixed with the electrolyte these pores help the electrolyte to soak into the interspaces and directly contact the crystalline grains, which improves the electrochemical performance of nickel hydroxide. Thus, it is concluded that samples A and B with high density exhibit different microstructures and surface properties due to different production processes, which may result in different electrochemical performances.

Fig. 2 represents a schematic diagram for the production of non-spherical $Ni(OH)_2$ using the PAM assisted two-step drying method and spherical $Ni(OH)_2$ prepared by the aforementioned "controlled crystallization" method. Experiments during the synthesis of the non-spherical $Ni(OH)_2$ have revealed that the effect of the coagulating agent (PAM) on tap-density, morphology, and surface properties of the non-spherical $Ni(OH)_2$ is significant. Addition of an appropriate amount of PAM into the $Ni(OH)_2$ suspension can greatly accelerate filtration rate and reduce the moisture content in the press cake, which results in agglomerations of colloid particles [22]. Coagulation further increases the structure's density, as the agglomerations squeeze out water. Due to this dense structure, the $Ni(OH)_2$ particles are prone to grow and crystallize in the subsequent drying process, and the tap-density of the $Ni(OH)_2$ thereby remarkably increases.

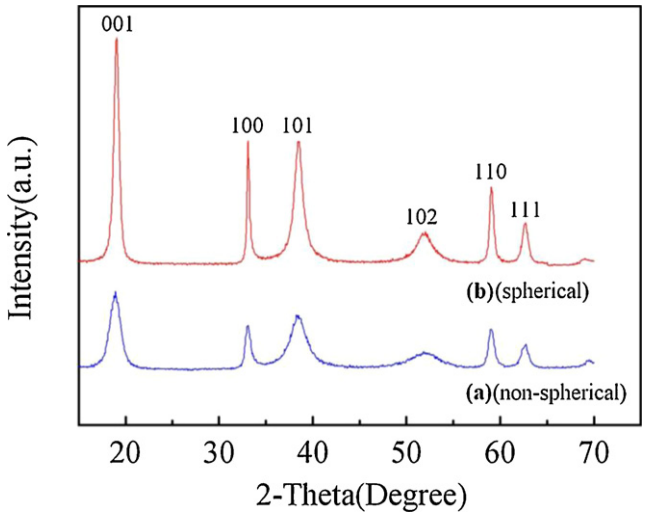

Fig. 3. XRD patterns of (a) non-spherical $Ni(OH)_2$ and (b) spherical $Ni(OH)_2$.

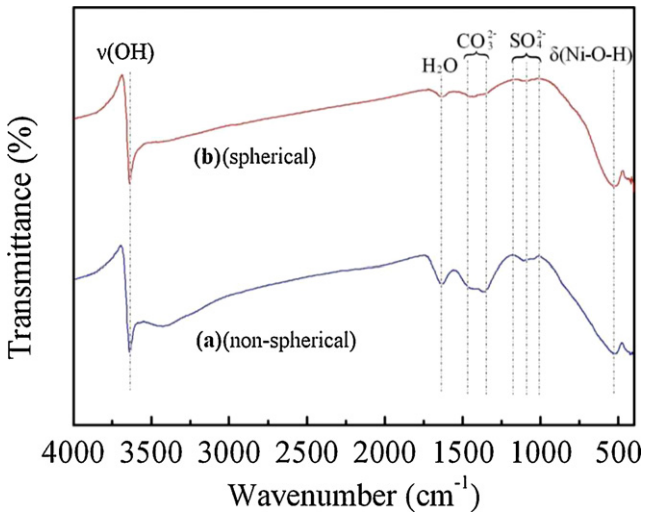

Fig. 4. IR spectra of (a) non-spherical $Ni(OH)_2$ and (b) spherical $Ni(OH)_2$.

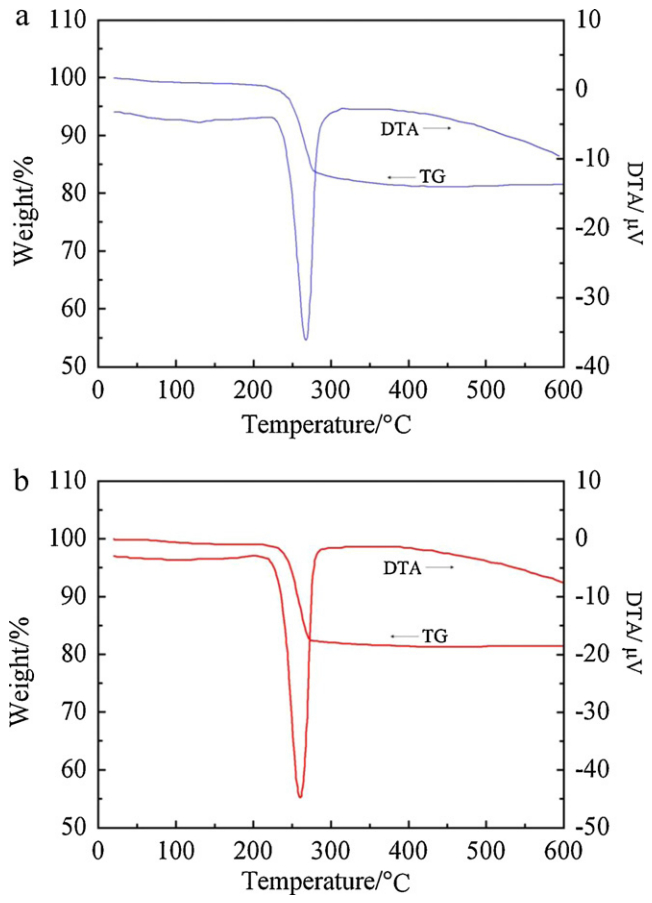

Fig. 5. TG and DTA curves for (a) non-spherical $Ni(OH)_2$ and (b) spherical $Ni(OH)_2$.

As shown in Fig. 2b, the production process of spherical $Ni(OH)_2$ is different from that of non-spherical powders, which involves a few steps: nucleation to form tiny particles, growth of tiny particles to form sheets or plates, and self-assembly and growth to form radial network structure [28]. Although the spherical shape can result in high-density, the crystal growth process for spherical particles requires a long time, the quality of the product cannot be guaranteed easily and the production cost is high. Consequently, the procedures for non-spherical $Ni(OH)_2$ powders are much simpler and more economical because there is no hydroxide-forming step, and are more environmentally friendly because no ammonium is involved.

3.1.3. XRD

The XRD patterns of $Ni(OH)_2$ samples A (non-spherical) and B (spherical) are presented in Fig. 3. The XRD patterns show that these two samples exhibit the β-$Ni(OH)_2$ phase characteristics with a brucite-type structure and a hexagonal unit, compared with the standard (JCPDS card No. 14-0117). No characteristic peaks corresponding to other phases are observed, but the width of the peaks is different. The broadening of some diffraction peaks [e.g. (0 0 1) and (h k 0)] in β-$Ni(OH)_2$ XRD patterns is directly related to the crystallite size [29]. The crystallite size perpendicular to various diffraction planes can be estimated from the XRD lines using the Scherrer formula [30,31]. The FWHMs and the d-values of the respective sample in the (0 0 1), (1 0 0), and (1 0 1) diffraction lines are listed in Table 2.

Table 3
Results of weight loss measurements for $Ni(OH)_2$ samples A (non-spherical) and B (spherical).

Weight loss region (°C)	Reason of weight loss	Sample	
		A (non-spherical)	B (spherical)
20–200	Dehydration	1.22%	0.96%
200–350	Dehydroxylation	17.15%	17.28%
350–600	Removal of intercalated anions	0.53%	0.29%

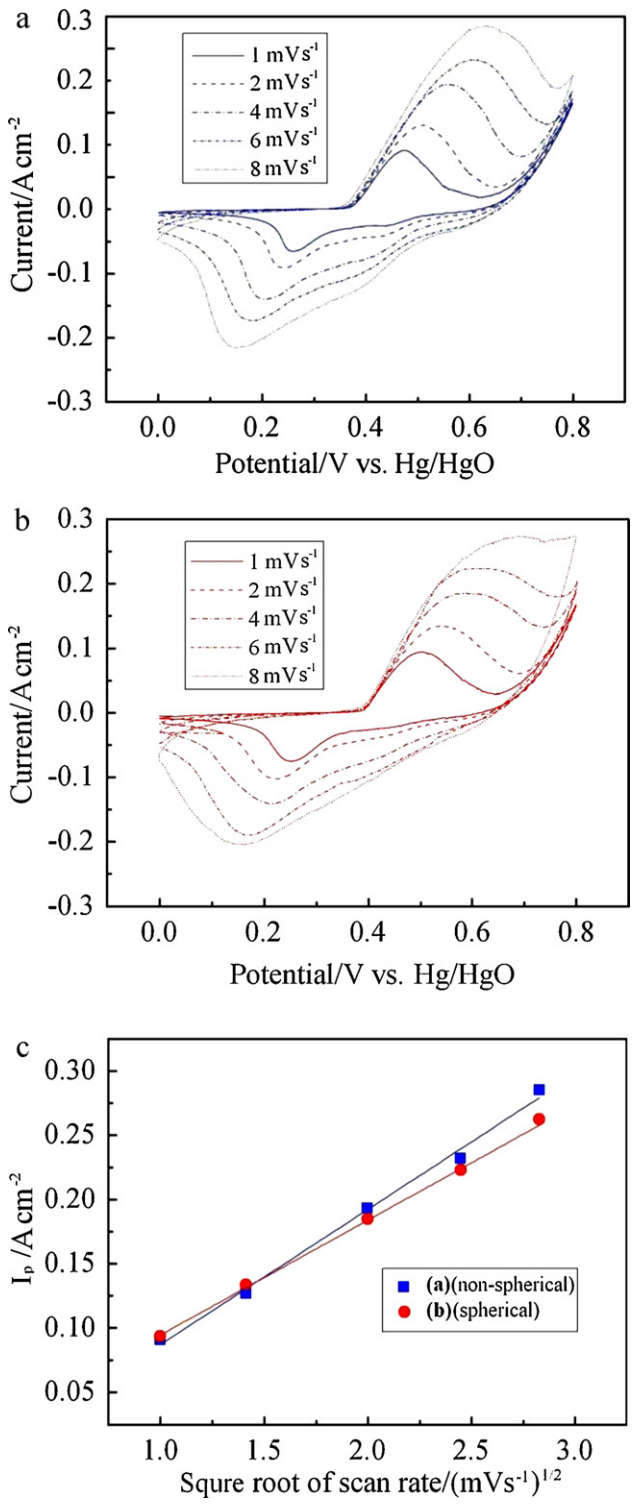

Fig. 6. Cyclic voltammograms of (a) non-spherical $Ni(OH)_2$ and (b) spherical $Ni(OH)_2$ at various scan rates. (c) Linear relationship between the cathodic peak current (I_p) and square root of scan rate for (a) non-spherical $Ni(OH)_2$ and (b) spherical $Ni(OH)_2$.

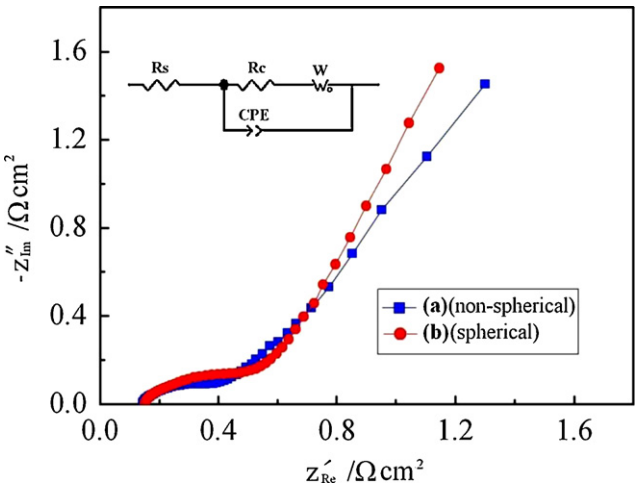

Fig. 7. Nyquist plots of (a) non-spherical $Ni(OH)_2$ and (b) spherical $Ni(OH)_2$.

As presented in Table 2, the FWHMs of the (0 0 1) and (1 0 0) diffraction lines of sample A are larger than those of sample B, indicating that the crystallite size of sample A is smaller than that of sample B. However, this result is not in accordance with the particle size results shown in Table 1, which may result from the different particle shapes.

It should be noticed that abnormal broadening of the (1 0 l) reflection lines ($l \neq 0$) cannot be attributed to the crystallite size alone. Structural disorder plays an important role in this broadening [32,33]. Structural disorder in $Ni(OH)_2$ can provide an easier path for the diffusion of protons within the NiO layers and can help lower the free energy by increasing the entropy, which can in turn increase the electrochemical reaction rate [10,12]. Previous reports have indicated that the peak (1 0 l) was especially broad when the nickel hydroxide was more active [34,35]. It is obvious that sample A shows a broader FWHM of the (1 0 1) diffraction line of 1.057, whereas the value for spherical sample B is 0.782, indicating that non-spherical powders possess a higher density of structural disorder and a better electrochemical activity in spite of its larger particle size.

3.1.4. IR spectra

Fig. 4 presents the infrared spectra of the as-prepared samples A (non-spherical) and B (spherical). Both IR spectra show similar characteristics. The strong, sharp band centered at 3640 cm^{-1} corresponds to the υ_{O-H} vibration, which is typical for β-$Ni(OH)_2$ [36]. The broad band at 3300 cm^{-1} is characteristic of the stretching vibration of the hydroxyl group extensively hydrogen bonded to water molecules and the band at 1650 cm^{-1} corresponds to the bending vibration of water molecules [37]. The couple bands at about 1470 cm^{-1} and 1380 cm^{-1} in both IR spectra can be assigned to $\upsilon_{c=o}$ vibration of the adsorbed CO_2 molecules due to the open system used for synthesis [38]. The band at about 1125 cm^{-1} corresponds to the vibration of SO_4^{2-} [39]. At low wave numbers, the bands at 460 cm^{-1} and 520 cm^{-1} are assigned to the bending vibration of υ_{Ni-O} and stretching vibration of υ_{Ni-OH}, respectively [40]. Notably, for sample A, the typical IR spectra characteristic of PAM are not found, indicating that PAM have been removed in the washing and drying process and do not affect the qualities of the products.

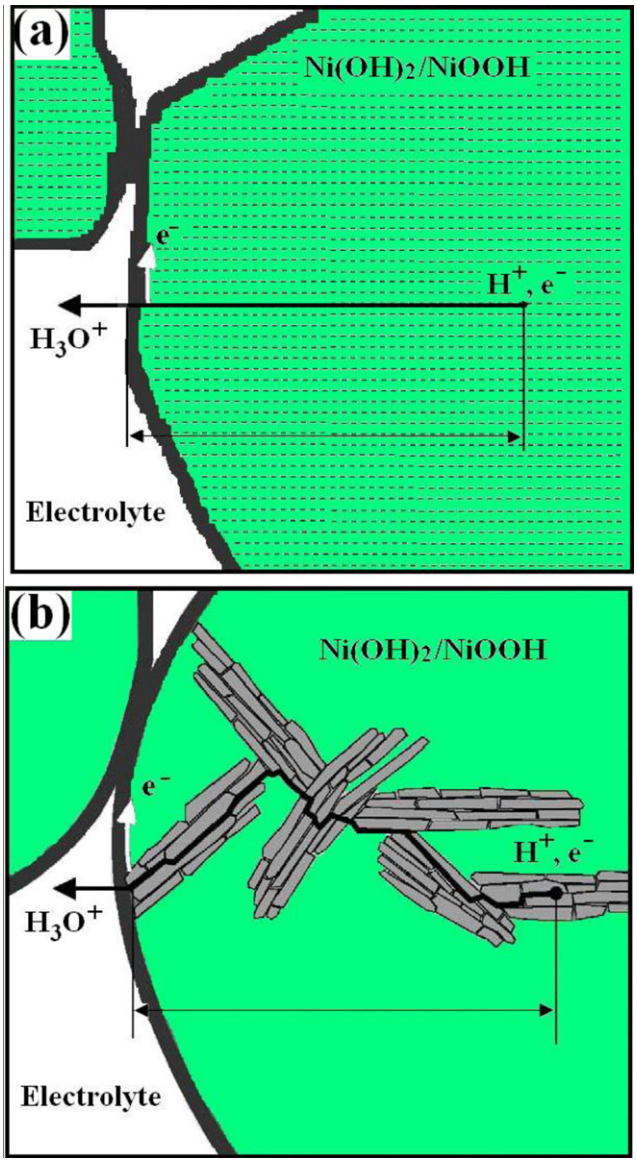

Fig. 8. Schematic drawing of proton/electron diffusion in (a) non-spherical $Ni(OH)_2$ and (b) spherical $Ni(OH)_2$.

3.1.5. TG–DTA

The TG and DTA curves for $Ni(OH)_2$ samples A (non-spherical) and B (spherical) are shown in Fig. 5 with detailed data listed in Table 3. Both samples A and B show three weight loss regions. The first region is below 200 °C, where the adsorbed water is removed. The second is between 200 °C and 350 °C, where the sample decomposes to NiO. The practical weight loss corresponding to this reaction, which can be estimated from the second weight loss step on the TG curves, is 17.15% and 17.29% for samples A and B, respectively. The third is between 350 °C and 600 °C, where the

Table 4
Parameters from CV and EIS measurements for non-spherical and spherical particles of $Ni(OH)_2$ paste electrode.

Sample	E_a (mV)	E_c (mV)	$\Delta E_{a,c}$ (mV)	E_{OER} (mV)	$E_{OER} - E_a$ (mV)	$E_{OER} - E_c$ (mV)	R_c (Ω cm^2)	W (Ω cm^2)	CPE (F cm^2)
A (non-spherical)	266	465	199	622	356	157	0.1428	0.4237	0.002767
B (spherical)	252	501	249	641	389	140	0.3938	0.6993	0.002248

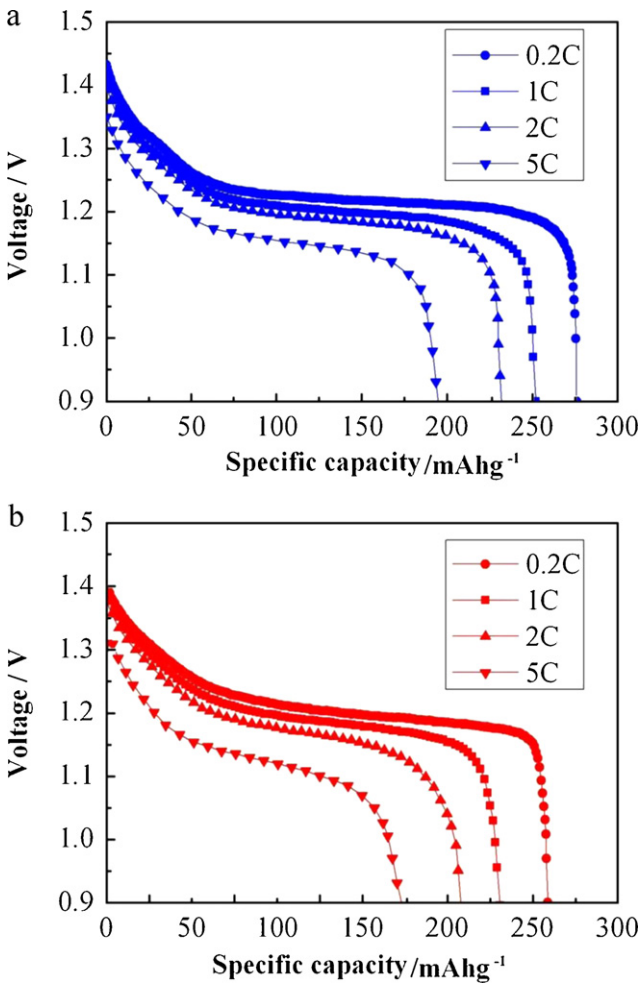

Fig. 9. Discharge curves of the electrodes prepared with (a) non-spherical $Ni(OH)_2$ and (b) spherical $Ni(OH)_2$ at different current rates.

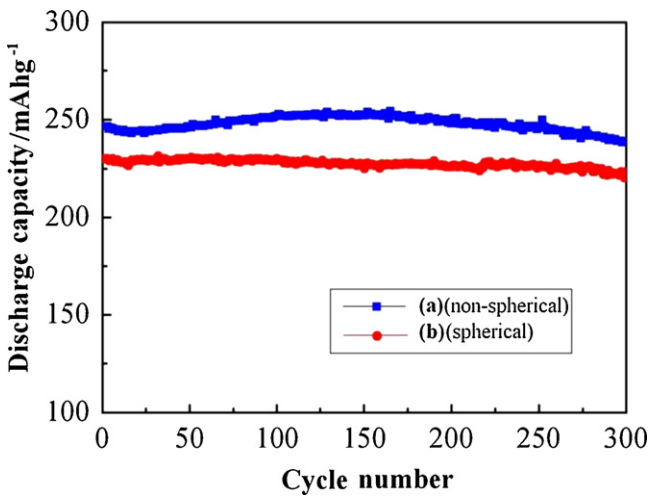

Fig. 10. Cyclic performance of the electrodes prepared with (a) non-spherical $Ni(OH)_2$ and (b) spherical $Ni(OH)_2$ at a 1 C charge/discharge rate.

intercalated anions are removed. The weight loss due to intercalation of anions was observed to be 0.53% for sample A, and 0.29% for sample B.

In Fig. 5, it can be seen that the temperatures corresponding to the decomposition reaction peaks on the DTA curves gradually decline, with readings of 267.76 and 259.97 °C for samples A and B, respectively. This indicates that the synthesized non-spherical $Ni(OH)_2$ powders are thermally more stable than spherical powders, as reflected in the lower decomposition reaction rate and higher decomposition temperature. Non-spherical $Ni(OH)_2$ powders have a higher thermal stability than spherical powders due to the dense solid structure and large particle size, although they have the same tap-density.

3.2. Electrochemical investigation of β-Ni(OH)$_2$

3.2.1. Cyclic voltammetry

Fig. 6 illustrates typical CV curves for samples A (non-spherical) and B (spherical) at various scan rates and 25 °C. Obviously, for both nickel electrodes, one anodic nickel hydroxide oxidation peak and one cathodic oxyhydroxide reduction peak are observable on the CV curves. To compare the CV characteristics of non-spherical and spherical particles, the results of CV measurements at a scan rate of 1 mV s^{-1} are tabulated in Table 4. The potential difference ($\Delta E_{a,c}$) between the anodic (E_a) and cathodic (E_c) peak potentials is taken as an estimate of reversibility of the redox reaction: the higher the reversibility, the smaller $\Delta E_{a,c}$ is [41,42]. The $\Delta E_{a,c}$ of non-spherical $Ni(OH)_2$ is much smaller than that of spherical one, indicating better reversibility of the electrochemical redox reaction in the non-spherical particles, thus more active material can be utilized during the charge/discharge process, which is proven by the charge/discharge results shown in Fig. 9. The charge process of the $Ni(OH)_2$ electrode usually occurs in competition with an oxygen evolution reaction (OER), which limits the electrochemical performance of the nickel hydroxide electrodes. As shown in Table 4, the potential difference between the oxygen evolution potential and the oxidation potential ($E_{OER} - E_c$) for the non-spherical sample is larger than that for spherical one. The large value allows the non-spherical sample to be charged fully before oxygen evolution, which can efficiently restrain the oxygen evolution reaction and improve the charge efficiency [42,43].

As is known, the electrochemical reaction process of a nickel hydroxide electrode is limited by the proton diffusion through the lattice [5,44]. Therefore, it is of great importance to study the nickel electrode's proton diffusion coefficient. The proton diffusion coefficient of the $Ni(OH)_2$ electrode was estimated based on the CV tests. Fig. 6c shows the relationship between the cathodic peak current (i_p) and the square root of the scan rate ($\nu^{1/2}$) for both nickel electrodes. The good linear relationship between i_p and $\nu^{1/2}$ suggests that the oxidation of nickel hydroxide is diffusion limited. In case of semi-infinite diffusion, the peak current i may be expressed by the Randles–Sevcik equation. At 25 °C, the peak current, i_p, in the cyclic voltammogram can be expressed as

$$i_p = 2.69 \times 10^5 \times n^{3/2} \times A \times D^{1/2} \times C_0 \times \nu^{1/2} \quad (1)$$

where n is the electron number of the reaction (≈1 for β-$Ni(OH)_2$), A is the geometrical surface area of the electrode in cm^2, D is the diffusion coefficient of H^+ in $cm^2\ s^{-1}$, ν is the scanning rate in V s^{-1}, and C_0 is the initial concentration of the reactant in mol cm^{-3}. For an $Ni(OH)_2$ electrode,

$$C_0 = \frac{\rho}{M} \quad (2)$$

where ρ and M are, respectively, the density and the molar mass (92.7 g mol^{-1}) of $Ni(OH)_2$. Using this equation and the slope of the fitted line in Fig. 6c, the proton diffusion coefficient for sample A is calculated to be $4.26 \times 10^{-9}\ cm^2\ s^{-1}$, which is larger than for sample B ($3.13 \times 10^{-9}\ cm^2\ s^{-1}$).

3.2.2. Electrochemical impedance spectroscopy (EIS)

Fig. 7 presents the electrochemical impedance spectra for electrodes A and B at a steady state. It can be seen that the Nyquist

plots of both electrodes display a semicircle resulting from charge transfer resistance in the high-frequency region, and a slope related to Warburg impedance in the low-frequency region [45,46]. In general, the slope in the low-frequency region is regarded as the Warburg slope, an empirical parameter related qualitatively rather than quantitatively to the diffusion resistance [45]. A high slope signifies a slow rate of diffusion, and a low slope a rapid rate of diffusion. The characteristics of the electrochemical system can be represented by the electrical equivalent circuit shown in the inset of Fig. 7, where R_s is the total resistance of the solution, CPE is the constant phase element related to the double layer capacity, R_c is the charge-transfer resistance of the electrode, and W is the generalized finite Warburg impedance (Z_W) of the solid phase diffusion [5]. The simulated values of the elements based on the equivalent circuit are listed in Table 4, where it can be seen that the R_c and W values of electrode A (Fig. 7a) are markedly lower than those of electrode B (Fig. 7b), which implies that the electrochemical reaction on electrode A proceeds more easily than on electrode B. Nevertheless, the CPE values of non-spherical particles are higher than spherical particles, which may be due to the fact that the as-prepared non-spherical $Ni(OH)_2$ has a larger effective active surface area for the electrochemical reactions. Thus, it proves that non-spherical particles have a lower resistance to charge-transfer and are more efficient for proton diffusion compared with spherical particles during the electrochemical reactions, and agrees with the results from CV measurements.

The high proton diffusion coefficient and low charge transfer resistance of non-spherical $Ni(OH)_2$ is attributable to its high structural disorder density, high specific surface area and compact structure. First, the high density of structural disorder for nickel hydroxide powder facilitates the solid-state proton diffusion in the $Ni(OH)_2$ lattice and helps diminish concentration polarization of the protons during the charge/discharge process, leading to a better charge/discharge cycling behavior [47]. Second, large specific surface area of non-spherical $Ni(OH)_2$ can provide a good interconnectivity network between the $Ni(OH)_2$ particles, and more chances for the particles to contact the electrolyte solution, therefore, proton diffusion is enhanced, which will in turn accelerate the electrode reaction. Last but not least, the high proton diffusion coefficient of non-spherical $Ni(OH)_2$ may be related to the different proton/electron diffusion routes in comparison with spherical $Ni(OH)_2$ particles. A schematic drawing to illustrate the proton/electron diffusion routes in (a) non-spherical $Ni(OH)_2$ and (b) spherical $Ni(OH)_2$ [48] is presented in Fig. 8.

For spherical $Ni(OH)_2$, Gille et al. [48] reported that during the charge/discharge process, although the diffusion route is geometrically not the shortest way, the proton/electron pairs tend to travel along the grain boundaries, surfaces or other areas of high atomic or lattice disorder due to dislocations or stacking faults in the active material of $Ni(OH)_2$/NiOOH, where the diffusion velocity of protons is assumed to be higher than that in the perfect lattice. For non-spherical $Ni(OH)_2$, we believe that the proton diffusion route is geometrically shorter because of the irregular particle shape and the dense solid structure, and the proton diffusion velocity is larger due to the high density of structural disorder in the active material of $Ni(OH)_2$/NiOOH, which results in a high proton diffusion coefficient.

3.2.3. Charge/discharge tests

Fig. 9 shows the discharge curves of nickel electrodes A (non-spherical) and B (spherical) at rates of 0.2, 1, 2, and 5 C, respectively. Obviously, sample A exhibits a larger discharge capacity and higher discharge potential plateau than sample B at the same discharge rate (0.2 C, 1 C, 2 C and 5 C). For example, at a rate of 0.2 C, the discharge capacity of sample A is 276.1 mAh g^{-1} in comparison with 259.3 mAh g^{-1} for sample B. As the discharge rate increases from 0.2 to 5 C, the discharge capacity of sample A decreases from 276.1 to 196.8 mAh g^{-1}, showing that at such a high discharge rate 71% of capacity is retained. Further, at a 5 C rate, the discharge capacity of sample A is 196.8 mAh g^{-1}, whereas the value for sample B is only 174.6 mAh g^{-1}, indicating that the high-rate performance of non-spherical $Ni(OH)_2$ is much better than that of spherical $Ni(OH)_2$.

The cyclic performance of nickel electrodes A (non-spherical) and B (spherical) at a 1 C rate is illustrated in Fig. 10. During the process of the charge/discharge cycles, electrode A shows a higher specific capacity and better cycling stability. During the cycling, the specific discharge capacity of electrode A increases, which reaches a maximum value after 152 cycles and then slowly decreases, whereas the specific discharge capacity of electrode B remains constant up to the maximum tested cycle (300th cycle). Especially, there is a higher capacity (11.5% more than corresponding spherical-$Ni(OH)_2$) for non-spherical particles in all cycles.

In summary, the overall electrochemical performance of the non-spherical, Co and Zn doped $Ni(OH)_2$ prepared by the new method is obviously superior to the commercial spherical $Ni(OH)_2$. This electrochemical performance improvement is attributable to the compact solid microstructure, high structural disorder density, large specific surface area of the non-spherical $Ni(OH)_2$, thus resulting in a better reaction reversibility, higher proton diffusion coefficient, and lower electrochemical impedance of the material, as indicated by CV and EIS.

4. Conclusions

This paper describes the effect of the microstructure and surface properties of $Ni(OH)_2$ on its electrochemical performance. Non-spherical, Co and Zn doped $Ni(OH)_2$ with a high tap-density was synthesized by the PAM assisted two-step drying method. Compared with commercial spherical $Ni(OH)_2$, the as-prepared $Ni(OH)_2$ particles exhibit an irregular tabular shape and a dense solid microstructure, which contains many overlapped sheet nano crystalline grains, and have a high density of structural disorder and a large specific surface area. The as-prepared non-spherical samples exhibit excellent electrochemical performance, which is markedly superior to the spherical β-$Ni(OH)_2$, such as better reaction reversibility, higher proton diffusion coefficient, lower charge transfer resistance, higher specific capacity, and better cyclic stability. The measured value of the proton diffusion coefficient for the non-spherical β-$Ni(OH)_2$ is 4.26×10^{-9} cm^2 s^{-1}, and the discharge capacity of the sample reaches 276 mAh g^{-1} at 0.2 C and about 196 mAh g^{-1} at 5 C. Therefore, it is believed that the non-spherical β-$Ni(OH)_2$ synthesized by the new method is a promising positive electrode active material for Ni–MH batteries.

Acknowledgements

This work is financially supported by the Natural Science Foundation of China under approval No. 21071046, and Henan Provincial Department of Science and Technology's Key Research Project under approval No. 080102270013.

References

[1] K. Watanabe, M. Koseki, N. Kumagai, J. Power Sources 58 (1996) 23.
[2] Z.R. Chang, H.W. Tang, J.G. Chen, Chem. Commun. 1 (1999) 513.
[3] U. Kohler, C. Antonius, P.B. Uerlein, J. Power Sources 127 (2004) 45.
[4] T.N. Ramesh, P. Vishnu Kamath, J. Power Sources 156 (2006) 655.
[5] M.A. Kiani, M.F. Mousavi, S. Ghasemi, J. Power Sources 195 (2010) 5794.
[6] Z.R. Chang, G.A. Li, Y.J. Zhao, J.G. Chen, Y.C. Ding, J. Power Sources 74 (1998) 252.
[7] W.G. Zhang, W.Q. Jiang, L.M. Yu, Z.Z. Fu, W. Xia, M.L. Yang, Int. J. Hydrogen Energy 34 (2009) 473.
[8] D.E. Reisner, A.J. Salkind, P.R. Strutt, T.D. Xiao, J. Power Sources 65 (1997) 231.
[9] J. Chen, D.H. Bradhurst, S. Dou, H. Liu, J. Electrochem. Soc. 146 (1999) 3606.

[10] W.K. Zhang, X.H. Xia, H. Huanga, Y.P. Gan, J.B. Wu, J.P. Tu, J. Power Sources 184 (2008) 646.
[11] G. Soler-Illia, M. Jobbágy, A. Regazzoni, M. Blesa, Chem. Mater. 11 (1999) 3140.
[12] J. Li, R. Li, J.M. Wu, H. Su, J. Power Sources 79 (1999) 86.
[13] S.A. Cheng, W.H. Leng, J.Q. Zhang, C.N. Cao, J. Power Sources 101 (2001) 248.
[14] X.J. Han, P. Xu, C.Q. Xu, L. Zhao, Z.B. Mo, T. Liu, Electrochim. Acta 50 (2005) 2763.
[15] H. Zhou, Z. Zhou, Solid State Ionics 176 (2005) 1909.
[16] L. Cao, F. Xu, Y.Y. Liang, H.L. Li, Adv. Mater. 16 (2004) 1853.
[17] J. Chen, N. Kuriyama, H. Yuan, H.T. Takeshita, T. Sakai, J. Am. Chem. Soc. 123 (2001) 11813.
[18] P. Jeevanandam, Y. Koltypin, A. Gedanken, Nano Lett. 1 (2001) 263.
[19] X.H. Liu, L. Yu, J. Power Sources 128 (2004) 326.
[20] X.M. He, J.J. Li, H.W. Cheng, C.Y. Jiang, C.R. Wan, J. Power Sources 152 (2005) 285.
[21] J.Q. Pan, Y.Z. Sun, Z.H. Wang, P.Y. Wan, Y.S. Yang, M.H. Fan, J. Power Sources 188 (2009) 308.
[22] E.B. Shangguan, Z.R. Chang, H.W. Tang, X.Z. Yuan, H.J. Wang, Int. J. Hydrogen Energy 35 (2010) 9716.
[23] R. Acharya, T. Subbaiah, S. Anand, R.P. Das, J. Power Sources 109 (2002) 494.
[24] P. Oliva, J. Leonardi, J.F. Laurent, C. Delmas, J.J. Braconnier, M. Figlarz, F. Fievet, A. de Guibert, J. Power Sources 8 (1982) 229.
[25] C. Tessier, C. Faure, L.G. Demourgues, C. Denage, G. Nabias, C. Delmas, J. Electrochem. Soc. 149 (2002) 1136.
[26] S. Deabate, F. Henn, Electrochim. Acta 50 (2005) 2823.
[27] T.N. Ramesh, J. Alloys Compd. 478 (2009) 12.
[28] M.X. Peng, X.Q. Shen, J. Cent. South Univ. Technol. 03 (2007) 0310.
[29] L. Indira, M. Dixit, P.V. Kamath, J. Power Sources 52 (1994) 93.
[30] K. Watanabe, N. Kumagai, J. Power Sources 76 (1998) 167.
[31] T.N. Ramesh, R.S. Jayashree, P. Vishnu Kamathz, J. Electrochem. Soc. 150 (2003) 520.
[32] M.C. Bernard, R. Cortes, M. Keddam, H. Takenouti, P. Bernard, S. Senyarich, J. Power Sources 63 (1996) 247.
[33] S. Deabate, F. Fourgeot, F. Henn, J. Power Sources 87 (2000) 125.
[34] C. Delmas, C. Tessier, J. Mater. Chem. 7 (1997) 1439.
[35] K. Watanabe, T. Kikuoka, N. Kumagai, J. Appl. Electrochem. 25 (1995) 219.
[36] L. Demourgues-Guerlou, C. Delmas, J. Power Sources 45 (1993) 281.
[37] Y.L. Zhao, J.M. Wang, H. Chen, T. Pan, J.Q. Zhang, C.N. Cao, Int. J. Hydrogen Energy 29 (2004) 889.
[38] C. Faure, Y. Borthomieu, C. Delmas, M. Fouassier, J. Power Sources 36 (1991) 113.
[39] N.V. Kosova, E.T. Devyatkina, V.V. Kaichev, J. Power Sources 174 (2007) 735.
[40] F. Portemer, A. Delahaye-Vidal, M. Figlarz, J. Electrochem. Soc. 139 (1992) 671.
[41] B. Liu, H.T. Yuan, Y.S. Zhang, Z.X. Zhou, D.Y. Song, J. Power Sources 79 (1999) 277.
[42] G.X. Yuan, K.L. Huang, S.Q. Liu, Y.J. Li, H.Y. Wang, J. Power Sources 195 (2010) 5094.
[43] W.H. Zhu, J.J. Ke, H.M. Yu, D.J. Zhang, J. Power Sources 56 (1995) 75.
[44] A.H. Zimmerman, P.K. Effa, J. Electrochem. Soc. 131 (1984) 709.
[45] M.A. Reid, P.L. Loyselle, J. Power Sources 36 (1991) 285.
[46] X.Y. Wang, J. Yan, H.T. Yuan, Y.S. Zhang, D.Y. Song, Int. J. Hydrogen Energy 24 (1999) 973.
[47] Q.S. Song, C.H. Chiu, S.L.I. Chan, Electrochim. Acta 51 (2006) 6548.
[48] G. Gille, S. Albrecht, J. Meese-Marktscheffel, A. Olbrich, F. Schrumpf, Solid State Ionics 148 (2002) 269.